



**Speciated atmospheric mercury at Waliguan Global Atmospheric Watch station
in the northeastern Tibetan Plateau: implication of dust related sources for
particulate bound mercury**

Hui Zhang¹, Xuewu Fu^{1,2*}, Ben Yu³, Baoxin Li⁴, Peng Liu⁴, Guoqing Zhang⁴, Leiming Zhang⁵,
Xinbin Feng^{1,2,6*}

¹ State Key Laboratory of Environmental Geochemistry, Institute of Geochemistry, Chinese Academy of Sciences,
99 Lincheng West Road, Guiyang, 550081, China.

² CAS Center for Excellence in Quaternary Science and Global Change, Xi'an, 710061, China.

³ State Key Laboratory of Environmental Chemistry and Ecotoxicology, Research Center for Eco-Environmental
Sciences, Chinese Academy of Sciences, Beijing, 100085, China.

⁴ China Global Atmosphere Watch Baseline Observatory, Qinghai Meteorological Bureau, Xining, 810001, China.

⁵ Air Quality Research Division, Science and Technology Branch, Environment and Climate Change Canada,
Toronto, M3H5T4, Canada

⁶ University of Chinese Academy of Sciences, Beijing, 100049, China.

Corresponding authors:

Xuewu Fu (fuxuewu@mail.gvig.ac.cn), Xinbin Feng (fengxinbin@vip.skleg.cn)



1 **Abstract**

2 To understand the ambient levels and sources of atmospheric mercury (Hg) in the Tibetan
3 Plateau, a full-year continuous measurement of speciated atmospheric mercury was conducted at
4 Waliguan (WLG) Baseline Observatory (3816 m a.s.l.) from May 2012 to April 2013. Mean
5 concentrations ($\pm 1SD$) of gaseous elemental mercury (GEM), gaseous oxidized mercury (GOM)
6 and particulate bound mercury (PBM) during the whole study period were $1.90 \pm 0.80 \text{ ng m}^{-3}$, 12.0
7 $\pm 10.6 \text{ pg m}^{-3}$ and $65.4 \pm 63.2 \text{ pg m}^{-3}$, respectively. Seasonal variations of GEM were very small,
8 while those of PBM were quite large with mean values being four times higher in cold (102.3 ± 66.7
9 pg m^{-3}) than warm ($22.8 \pm 14.6 \text{ pg m}^{-3}$) season. Anthropogenic emissions to the east of Tibetan
10 Plateau contributed significantly to GEM pollution at WLG, while dust particles originated from
11 desert and Gobi regions in Xinjiang province and Tibetan Plateau to the west of WLG were
12 responsible to PBM pollution at WLG. This finding is also supported by the significant positive
13 correlation between daily PBM concentration and daily cumulative absorbing aerosol index (AAI)
14 encountered by air masses transported during the preceding two days.

15
16 **Keywords:** Speciated atmospheric mercury, Particulate bound mercury, Anthropogenic mercury
17 emissions, Dust related sources

18
19 **Introduction**

20 Mercury (Hg) is a toxic pollutant of global concern due to its long lifetime in air,
21 bioaccumulation in aquatic system, and detrimental impacts on human and animal health.
22 Atmospheric Hg is operationally defined in three forms, i.e., gaseous elemental mercury (GEM),
23 gaseous oxidized mercury (GOM), and particulate bound mercury (PBM). These Hg species can be
24 transformed among each other through complex physical and chemical processes (Lyman et al.,
25 2020; Selin, 2009). For example, GEM can be oxidized to form GOM, and GEM and/or GOM can
26 adsorb on atmospheric aerosols to form PBM. GEM has a lifetime in air of 0.5-2 years while GOM
27 and PBM only have a lifetime of hours to weeks (Ariya et al., 2015; Murphy et al., 2006). Because
28 of their different lifetimes, GEM can be transported globally via atmospheric circulation whereas
29 PBM is limited to regional transport (Pirrone et al., 2010). These Hg species can be removed from
30 the atmospheric through dry and wet deposition processes. Once deposited to earth's surface, Hg
31 can be converted to methylmercury by biological processes, which can cause potential risks to
32 ecological and human health (Jonsson et al., 2014; Wright et al., 2018). On the other hand, Hg
33 accumulated in soil and water bodies can be emitted into the atmosphere, which plays an important
34 role in the global atmospheric Hg cycle (Obrist et al., 2018; Wang et al., 2016).

35



36 Spatiotemporal variations of atmospheric Hg and Hg speciation fractions within the total Hg
37 are controlled by many factors, among which anthropogenic emissions are important ones (Driscoll
38 et al., 2013; Fu et al., 2012b). Global anthropogenic Hg emissions to the atmosphere were estimated
39 to be 2224 Mg yr⁻¹, of which 82-87%, 10-18% and 3-4% were in the form of GEM, GOM and PBM,
40 respectively (AMAP/UNEP 2018). In China, concentrations of GEM and PBM were generally
41 elevated compare to the observations in Europe and America. The fractions of PBM in total
42 atmospheric Hg in urban areas of China were in the range of 5.2–17.2%, higher than those from
43 total anthropogenic Hg emissions (Fu et al., 2015; Zhang et al., 2015b). In addition, observations of
44 speciated atmospheric Hg in China in both urban and rural areas of China showed generally higher
45 PBM than GOM levels (Fu et al., 2015b), which is in contrast with the higher GOM than PBM
46 fractions in the total anthropogenic Hg emissions in China (Zhang et al., 2015b). These findings
47 indicate that additional emission sources and other physical and chemical processes contributed to
48 the elevated PBM concentrations in China. For example, natural sources, such as biomass burning
49 and dust related sources, and gas-particle partitioning can also produce PBM (Amos et al., 2012;
50 Obrist et al., 2008). The impact of these sources and processes on atmospheric PBM, although is
51 potentially important, has not been well investigated by previous studies.

52

53 Speciated atmospheric Hg has been monitored in China in recent years, but observations in the
54 Tibetan Plateau region are very limited. The Tibetan Plateau, also known as the third pole of the
55 world with an average altitude of over 4000 m a.s.l., is an ideal place for assessing transport and
56 transformation of atmospheric pollutants in China and other Asian regions (Chen et al., 2019;
57 Loewen et al., 2007). The Tibetan Plateau is surrounded by East Asia and South Asia, which are the
58 two most important source regions of atmospheric Hg in the world (Zhao et al., 2013). The
59 Taklamakan and Gobi deserts are located to the west and north, respectively, of the Tibetan Plateau.
60 Since the Tibetan Plateau region is strongly impacted by westerlies, Indian Summer Monsoon and
61 East Asia Summer Monsoon (Fig.1), it is affected by air pollutants from anthropogenic and natural
62 source regions adjacent to the Tibetan Plateau (Che et al., 2011). Previous studies postulated that air
63 masses passing over the urban and industrial areas in western China and South Asia were important
64 sources of atmospheric GEM at Waliguan and Nam Co (4730 m a.s.l.) on the northeastern edge and
65 Midlands of the Tibetan Plateau, respectively (Fu et al., 2012a; Yin et al., 2018). At Shangri-La,
66 located on the southeastern edge of the Tibetan Plateau, the identified atmospheric GEM source
67 regions were also located in Southeast Asia and mainland China (Zhang et al., 2015a). Speciated
68 atmospheric Hg measurement was only carried out during a warm season in Qomolangma Natural
69 Nature Preserve (4276 m a.s.l.) of Tibetan Plateau (Lin et al., 2019). Low GEM concentrations
70 (means: 1.33 to 1.42 ng m⁻³), but elevated PBM concentrations (means: 25.6 to 49.0 pg m⁻³), were



71 observed in middle and southern Tibetan Plateau as compared to those in rural central and eastern
72 China (Yin et al., 2018; Lin et al., 2019). To date, long-term observations of speciated atmospheric
73 Hg in the Tibetan Plateau region are still lacking, limiting our capacity to fully understand the
74 spatiotemporal patterns of Hg in this region and associated source regions and controlling factors.

75

76 In this study, one-year continuous monitoring of speciated atmospheric Hg was carried out at
77 WLG in Tibetan Plateau region. Data were analyzed carefully for exploring the ambient levels,
78 seasonal and diurnal patterns, and source regions of speciated atmospheric Hg in this region.
79 Knowledge generated from this study is needed for establishing future emission control policies in
80 order to preserve many sensitive ecosystems in this region.

81

82 **2 Materials and methods**

83 **2.1 Measurement site**

84 The measurement site is situated at the summit of Mt. Waliguan located at northeastern edge
85 of the Tibetan Plateau in northwest China. It is a station known as Waliguan (WLG) Baseline
86 Observatory (100°54' E, 36°17' N, 3816 m a.s.l.) (Fig. 1), which is the only station in inner Asia in
87 the Global Atmospheric Watch (GAW) program of World Meteorological Organization (WMO).
88 This area has a typical high plateau continental climate, and western winds dominant at the site (Fu
89 et al., 2012a; Okamoto and Tanimoto, 2016; Xu et al., 2018). WLG is mainly surrounded by the arid
90 and semi-arid grassland and desert lands. The population density is very low and industrial activities
91 sparsely distributed within 80 km around WLG. Anthropogenic Hg emissions in Qinghai province
92 is relatively low, and are mostly located to the east of WLG (Fu et al., 2015; Sun et al., 2020; Wu
93 et al., 2006). The Taklimakan Desert and Gobi Desert of Xinjiang province are located to the west
94 of WLG, and the Gobi Desert of Hexi Corridor and southern Inner Mongolia are located to the north
95 of WLG (Fig.1).

96

97 **2.2 Sampling method**

98 **2.2.1 Measurements of speciated atmospheric mercury**

99 High-temporal resolution measurements of GEM, GOM and PBM were carried out using the
100 2537B-1130-1135 Atmosphere Speciation Mercury Analysis System (Fig. 1, Tekran Inc., Toronto,
101 Canada) from May 2012 to April 2013. The Tekran Model 2537B Mercury Vapour Analyzer
102 provides continuous analysis of GEM in air at 0.1 ng m⁻³ detection limit. The instrument samples
103 air and captures vapour phase Hg on the cartridges containing ultra-pure gold adsorbent media. The
104 amalgamated Hg is thermally desorbed and detected using Cold Vapour Atomic Fluorescence
105 Spectrometry (CVAFS). The Model 1135 Particulate Mercury Unit, together with the Model 1130



106 Mercury Speciation Unit, allows the Model 2537B Mercury Vapor Analyzer to simultaneously
107 monitor and differentiate between GEM, GOM and PBM (fine fraction, < 2.5 μm) in ambient air.
108 KCl-coated annular denuders was installed in the specially designated location of Model 1130
109 Mercury Speciation Unit before the instrument starts running. The instrument's workflow is
110 controlled by the controller which is capable of executing an automatic sampling and analysis
111 program (Feng et al., 2000; Fu et al., 2016; Lindberg et al., 2002). This system has been used to
112 monitor atmospheric Hg species worldwide, including the North America Atmospheric Mercury
113 Network (AMNet) and the Global Mercury Observation System (GMOS) (Lan et al., 2012;
114 Sprovieri et al., 2016). In this study, data QA/QC procedure followed the GMOS Standard Operation
115 Procedure and Data Quality Management (D'Amore et al., 2015). Although KCl-coated annular
116 denuders have been the most popular and widely applied method for measuring ambient GOM,
117 large analytical uncertainties in GOM may exist due to the trace level and complicated chemical
118 compounds of GOM which may not be fully collected by denuders (Ariya et al., 2015; Cheng and
119 Zhang, 2017; Gustin et al., 2015; Gustin et al., 2019). Analysis and discussions presented in this
120 study are mostly focused on GEM and PBM, considering the larger uncertainties in GOM than GEM
121 and PBM.

122

123 2.2 Meteorological data and backward trajectory calculation

124 Meteorological parameters, including air temperature (AT), relative humidity (RH), rainfall
125 (RF), wind direction (WD) and wind speed (WS) were obtained from the local weather station at
126 WLG. In order to identify the effect of long-range transport of Hg emissions on the distributions of
127 atmospheric Hg at WLG, backward trajectories arriving the site at 100 m above the ground were
128 calculated every 4 hours using the TrajStat software and gridded meteorological data from the Air
129 Resource Laboratory, National Oceanic and Atmospheric Administration (NOAA) (Wang et al.,
130 2009). To investigate the source regions potentially influencing GEM and PBM concentrations at
131 WLG, a weighing algorithm based on measured concentrations, known as the concentration
132 weighted trajectory (CWT) approach, was applied in this study. In this procedure, the CWT value
133 indicates the source strength of a $0.5^\circ \times 0.5^\circ$ grid cell (CWT_{ij}) to the WLG and is defined as:

$$134 \quad C_{ij} = \frac{1}{\sum_{l=1}^M \tau_{ijl}} \sum_{l=1}^M C_l \tau_{ijl}$$

135 where C_{ij} is the average CWT value of speciated atmospheric Hg in the grid cell (i,j), C_l is the
136 measured Hg concentration at WLG, τ_{ijl} is the number of trajectory endpoints in the grid cell (i,j)
137 associated with the C_l sample, and M is the number of samples that have trajectory endpoints in grid
138 cell (i,j). A point filter is applied as the final step of CWT to eliminate grid cells with few endpoints.
139 Weighted concentration fields show concentration gradients across potential sources. This method



140 helps determine the relative significance of potential source regions (Cheng et al., 2013; Zhang et
141 al., 2016).

142

143 **2.3 Ancillary parameters and analysis**

144 Anthropogenic emissions of GEM and PBM in $0.5^\circ \times 0.5^\circ$ grid cells in the studied domain
145 were obtained from the 2010 global emission dataset developed by the Arctic Monitoring and
146 Assessment program (AMAP) (AMAP/UNEP, 2013). Gridded monthly biomass burned areas at
147 0.25° spatial resolution were obtained from the fourth version of the Global Fire Emission Database
148 (GFED4) (Giglio et al., 2013). Absorbing Aerosol Index (AAI) constitutes one of the most useful
149 space-borne data sets, offering temporal and spatial information on UV absorbing aerosols (black
150 carbon, desert dust) distributions. Desert dust and biomass burning related aerosols are the dominant
151 aerosol types detected by the AAI, and AAI is therefore a useful parameter for qualitatively
152 identifying the dust and biomass burning related sources. The AAI data are available on daily and
153 monthly basis at a spatial resolution of 1×1 degree. Generally, non-absorbing aerosols (e.g., sulfate
154 and sea-salt) yield negative AAI values, UV-absorbing aerosols (e.g., dust and smoke) yield positive
155 AAI values, and clouds yield near-zero values (Prospero et al., 2002). Such information can be used
156 for identifying distinct desert dust aerosol sources and analyzing dust and smoke transport patterns
157 (Chiapello et al., 1999; Kubilay et al., 2005; Moulin and Chiapello, 2004). A detailed description of
158 the AAI product is given in (Herman et al., 1997; Torres et al., 1998). In this study, Global monthly
159 gridded (1×1 degrees) AAI products during our study period were obtained from the Tropospheric
160 Emission Monitoring Internet Service (TEMIS) (<http://www.temis.nl/airpollution/absaa/>).

161

162 To study the effect of dust related sources on the variations in PBM concentration at WLG, we
163 calculated the daily cumulative AAI (Σ AAI) based on the 2-day backward trajectory and gridded
164 AAI data. Further analysis between the daily Σ AAI and mean PBM concentration were conducted
165 to assess the effect of dust related sources on the variations of PBM at WLG.

166

167 **3 Results and discussion**

168 **3.1 Concentrations of GEM, GOM and PBM**

169 Time series of hourly speciated atmospheric Hg concentrations is shown in Fig.2. Mean (± 1 sd)
170 concentrations of GEM, GOM and PBM at WLG during the whole sampling campaign were $1.85 \pm$
171 0.96 ng m^{-3} , $14.0 \pm 13.2 \text{ pg m}^{-3}$ and $68.1 \pm 70.3 \text{ pg m}^{-3}$, respectively. Mean GEM level at WLG was
172 relatively higher than the background levels in the Northern Hemisphere ($1.5\text{-}1.7 \text{ ng m}^{-3}$) (Fu et al.,
173 2015; Sprovieri et al., 2016). Mean GEM concentration at WLG was relatively lower than that
174 observed in Mt. Gongga (mean = $3.98 \pm 1.62 \text{ ng m}^{-3}$, 1sd) and Shangri-La (mean = $2.55 \pm 0.73 \text{ ng}$



175 m^{-3} , 1sd) located on the eastern edge of the Tibetan Plateau, but much higher than that observed in
176 Qomolangma Natural Nature Preserve (mean = $1.42 \pm 0.37 \text{ ng m}^{-3}$, 1sd) and Nam Co (mean = 1.33
177 $\pm 0.24 \text{ ng m}^{-3}$, 1sd) in the inland Tibetan Plateau (Fu et al., 2012b; Fu et al., 2009; Lin et al., 2019;
178 Yin et al., 2018; Zhang et al., 2015a). In general, atmospheric GEM levels in remote areas are closely
179 related to the regional atmospheric Hg budget. The inland Tibetan Plateau is sparsely populated and
180 with no large-scale industrial activities. However, Some monitoring sites on the northeastern and
181 eastern edges of the Tibetan Plateau, such as WLG, Mt. Gongga and Shangri-La, are not too far
182 away from the anthropogenic Hg source regions in middle and eastern China, and thus were
183 impacted by anthropogenic Hg emissions through long-range transport, which explained the
184 relatively higher GEM concentrations at these stations than inland Tibetan Plateau stations (Fu et
185 al., 2008; Zhang et al., 2015a). The impact of regional and long-range transport of Hg originated
186 from anthropogenic emissions on the elevated GEM level at WLG was discussed in details in section
187 3.3 below.

188

189 Currently, there is a great debate on the measurement accuracy of GOM using KCl-coated
190 denuder. Therefore, GOM data in this study was only compared with previously reported data
191 collected using the same method. The mean GOM concentration at WLG was slightly higher than
192 those in rural areas of North America and China, but lower than those in urban areas in China (Fu
193 et al., 2012b; Zhang et al., 2016). GOM is mainly affected by local to regional emission sources and
194 atmospheric processes (Sheu and Mason, 2001). Since WLG is isolated from primary anthropogenic
195 sources, the relatively high level of GOM at WLG was probably mainly caused by atmospheric
196 processes. Intrusion of GOM enriched air from free troposphere could be one reason, a phenomenon
197 that has been reported in Qomolangma Natural Nature Preserve in the southern Tibetan Plateau (Lin
198 et al., 2019). Additionally, GOM at WLG generally showed relatively higher concentrations during
199 daytime (Fig. S1), indicating in situ photochemical production of GOM as another important
200 mechanism causing high GOM levels at WLG.

201

202 PBM concentrations at WLG showed large variations with the maximum hourly value reaching
203 655 pg m^{-3} . The overall mean PBM concentration at WLG (68.1 pg m^{-3}) was significantly higher
204 (by up to ~ 5 -40 times) than those reported for remote areas in the northern Hemisphere (Kim et al.,
205 2012; Lan et al., 2012), but was similar to observations in the urban areas in China (Fu et al., 2012b;
206 Fu et al., 2015). Elevated PBM concentrations in Chinese urban areas were most likely caused by
207 strong local anthropogenic emissions. However, in the remote areas with few primary anthropogenic
208 emissions, long-range transport should be the major cause for highly elevated PBM concentrations.
209 PBM has an atmospheric residence time ranging from a few days to weeks and can undergo regional



210 transport (Seigneur et al., 2004; Zhang et al., 2019). Therefore, high PBM levels at WLG were
211 probably mainly caused by long-range transport of anthropogenic and natural emissions, which was
212 discussed in details in the following Sections.

213

214 3.2 Seasonal and diurnal distributions of GEM, GOM and PBM

215 Daily values of GEM, GOM, PBM, AT, RH, WS and RF were aggregated into monthly
216 average values to reveal seasonal variations during the study period (Table S1 and Fig.3). In the
217 discussion below, warm (May to October) and cold (November to April) seasons were compared.
218 Mean GEM level in the cold season (1.84 ng m^{-3}) was relatively lower than that in the warm season
219 (1.95 ng m^{-3}) (Table S1), which was likely due to the strengthening westerlies originated from or
220 passing over regions with low anthropogenic emissions during the cold season (Zhang et al., 2015b).
221 However, higher than seasonal-average GEM levels were observed during February to April (Table
222 S1), likely due to the long-range transport from northern South Asia where has been experiencing
223 industrialization and urbanization and thus strong anthropogenic Hg emissions (AMAP/UNEP,
224 2018; Chakraborty et al., 2013). Airflows originated from these areas had high GEM concentrations
225 and could be transported to WLG in the cold season (Lin et al., 2019; Yin et al., 2018). In addition,
226 higher than seasonal-average GEM concentrations were also observed during July to September
227 (Table S1, Fig.3), which could be attributed to the strengthening East Asia Summer Monsoon during
228 the warm season. The prevailing wind from the east direction (Fig.4, Table S1) could transport GEM
229 from eastern Qinghai and southern Gansu province of China to WLG during the East Asian Summer
230 Monsoon season.

231

232 Unlike GEM, mean GOM and PBM concentrations were higher in the cold than warm season
233 (Table S1, Fig.3), which should be mainly caused by the efficient precipitation scavenging of GOM
234 and PBM due to high RF in the warm season. In addition, the low RH in the cold season was
235 conducive to the formation of GOM and PBM through atmospheric chemical and physical
236 transformations (Fain et al., 2009; Lin et al., 2019). Higher PBM concentrations at WLG were
237 frequently detected with westerly and northerly winds (Fig. 4), which were mainly from the desert
238 and Gobi areas of western Tibetan Plateau, Xinjiang, southern Gansu and southwestern Inner
239 magnolia, suggesting that desert dust related sources in these regions could be potential sources of
240 PBM at WLG in the cold season.

241

242 No significant differences in GEM concentration were observed between daytime (7:00-19:00,
243 1.86 ng m^{-3}) and nighttime (20:00-06:00, 1.83 ng m^{-3}) at WLG (Fig.S1). This was also the case for
244 PBM (72.2 pg m^{-3} versus 69.8 pg m^{-3}). The diurnal pattern of PBM at WLG was different from those



245 observed in Nam Co, Qomolangma Natural Nature Preserve and Mt. Gongga in the Tibetan Plateau
246 where PBM generally peaked during daytime under valley breeze condition (Fu et al., 2009; Lin et
247 al., 2019; Yin et al., 2018). The above findings at WLG suggested that local sources and in situ
248 atmospheric transformations may only have minor impacts on PBM concentration. Instead,
249 atmospheric circulation over the Tibetan plateau and long range transport from the other source
250 regions should be the main factors controlling the diurnal and seasonal variations of GEM and PBM
251 concentrations at WLG. In contrast, mean concentration of GOM during daytime (15.8 pg m^{-3}) was
252 27% higher than that during night (12.4 pg m^{-3}) at WLG, which was likely due to the oxidation of
253 GEM during the daytime (Ariya et al., 2015; Fain et al., 2009). Therefore, local meteorology and
254 photochemical production could be important controlling factors for the observed diurnal patterns
255 of GOM at WLG.

256

257 3.3 Source identification of GEM and PBM

258 During the whole study period, the prevailing winds at WLG were from southwestern quadrant
259 (46.5%) mainly originated from and passing over Tibetan Plateau and southern Xinjiang under the
260 control of the westerlies. Average GEM concentrations (1.58 to 1.91 ng m^{-3}) associated with this
261 wind sector were overall lower than those associated with other wind sectors (Fig. 4), suggesting
262 the areas southwest of WLG were not important source regions of GEM at WLG. In contrast, GEM
263 concentrations (means: 2.42 to 2.87 ng m^{-3}) associated with northeast wind sector were highly
264 elevated. The northeast wind mainly came from the low-altitude regions in northwestern China with
265 many anthropogenic Hg sources, which could have contributed to GEM at WLG. In contrast to
266 GEM, maximum PBM concentrations (means: 68.6 to 97.8 pg m^{-3}) were associated with wind
267 sectors of southwestern and northwestern quadrants and lowest PBM concentrations (means: 49.6
268 to 63.3 pg m^{-3}) were associated with wind sector of the eastern quadrants (Fig. 4). The southwest
269 and northwest winds were mainly originated from and passed over deserts and Gobi regions,
270 including the largest Taklimakan Desert in Asia. These areas are the main dust source regions in
271 middle and eastern China (Che et al., 2011; Chen et al., 2017), and therefore would be an important
272 source of PBM at WLG.

273

274 To better understand the sources and long-range transport of atmospheric Hg at WLG, CWT
275 values for GEM and PBM were calculated and are shown in Fig. 5. Higher GEM CWT values were
276 mainly located in eastern Qinghai, southern Gansu, western Shanxi, and southwestern Inner
277 Mongolia of China and northern South Asia, whereas lower values were mainly located western
278 Qinghai, Xinjiang and Xizang provinces (Fig. 5a). By matching the gridded GEM CWT values with
279 the gridded anthropogenic GEM emissions in the study domain, we found GEM CWT values were



280 significantly positively correlated with anthropogenic GEM emissions ($R^2 = 0.55, p < 0.01$, Fig. 6a).
281 This indicates GEM at WLG was mainly caused by long-range transport of anthropogenic GEM
282 emissions from industrial areas in western China, and this is overall consistent with the findings
283 discussed above that were based on wind dependence of GEM at WLG.

284

285 Differing from the case of GEM, higher PBM CWT values were mainly located in southern
286 Xinjiang, western Qinghai and south-central Xizang provinces, whereas the regions to the east of
287 WLG, where many industrial sources were located, showed relatively lower PBM CWT values (Fig.
288 5b). In addition, gridded PBM CWT values showed a negative correlation with gridded
289 anthropogenic PBM emissions (Fig. 6b). These findings indicate that long-range transport of
290 anthropogenic PBM emission was unlikely the major sources of PBM at WLG. Instead, long-range
291 transport of dust particles originated from deserts and Gobi regions in western China, such as
292 Taklimakan desert, Qaidam desert and Badain Jaran desert (Fig. S2), is responsible for PBM at
293 WLG. These regions contain the major deserts and Gobi areas in East Asia and can release up to 25
294 million tons dust particles annually. Dusts from these regions could be transported to the
295 northwestern, middle and even eastern China through the westerlies over the Tibetan plateau (Che
296 et al., 2011; Chen et al., 2017; Xuan et al., 2000). Previous studies showed that atmospheric PBM
297 concentrations ($86.1\text{-}517 \text{ pg m}^{-3}$) over the Taklimakan Desert are remarkably higher than those
298 observed from background sites in China and even comparable to those measured in most of the
299 Chinese metropolitan cities (Huang et al., 2020). We thus concluded that the dry airflows transported
300 the PBM-enriched dust aerosols from the desert and Gobi regions to WLG, and contributed
301 significantly to the elevated PBM concentrations at WLG.

302

303 **3.4 Impact of desert dust related sources on PBM**

304 To evaluate the impact of dust related sources on the temporal variations of PBM concentration,
305 daily cumulative AAI ($\sum\text{AAI}$) encountered by air masses transported during the preceding two days
306 were calculated, as shown in Fig. 7 together with daily PBM concentrations. PBM concentrations
307 maintained at relatively low levels in warm months (May to September), increased since October,
308 and reached the highest levels in winter and early spring (December to March) (Table S1). Daily
309 $\sum\text{AAI}$ showed negative values from June to October, but large positive values in winter and early
310 spring (Table S1 and Fig. 7). A significant positive correlation ($r^2 = 0.31, p < 0.01$) was observed
311 between daily $\sum\text{AAI}$ and daily PBM concentration (Fig. 7), indicating that the long-range transport
312 of dust and/or biomass burning related sources played an important role in the temporal variations
313 of PBM concentration at WLG. Biomass burning related sources were not likely the major causes
314 because the air masses ended at WLG were mainly originated from and passed over regions with



315 low biomass burning area (Fig. S2). Hence, we conclude that dust related sources were the dominant
316 source of PBM at WLG. Previous studies analyzing spatiotemporal patterns of atmospheric dust
317 based on satellite remote sensing generated dust aerosol index have shown the Taklimakan area as
318 the dominant source of dust episodes in Asia, especially in every spring season. Desert dust is a
319 significant carrier of atmospheric aerosol and PBM to the cryosphere of Western China and can also
320 have global impact through long-range transport (Huang et al., 2020; Zhang et al., 2008).

321

322 Desert and Gobi areas are important sources of atmospheric particles. Global dust particle
323 emissions were estimated to range from 500 to 5000 Tg yr⁻¹ with an average value of 1836±903 Tg
324 yr⁻¹. In China, the desert and Gobi dust particle emissions were estimated to range from 100 to 459
325 Tg yr⁻¹ with an average value of 242±120 Tg yr⁻¹ (Table S2). Hg content in suspended particles from
326 desert dust was averaged at 0.33 µg g⁻¹ from existing studies (Table S2). Based on the above
327 numbers, PBM emissions from desert dust were roughly estimated to be 606 ± 298 Mg yr⁻¹ globally
328 and 80 ± 40 Mg yr⁻¹ in China. These values exceed the anthropogenic PBM emissions in the world
329 (75 Mg yr⁻¹) and China (16 Mg yr⁻¹), suggesting desert and Gobi areas as important sources of
330 atmospheric PBM emissions on regional to global scales.

331

332 Besides emissions from anthropogenic and dust related sources, gas-particle partitioning
333 between GOM and PBM also affect PBM level in the atmosphere. Thus, the intrusion of GOM-rich
334 air from free troposphere would also have an impact on PBM (Ariya et al., 2015; Lin et al., 2019;
335 Tsamalis et al., 2014). The PBM/GEM ratios at WLG were similar to those observed at
336 Qomolangma Natural Nature Preserve and Nam Co. in the Tibetan Plateau, but much higher than
337 those in Chinese urban and remote areas (Lin et al., 2019; Yin et al., 2018). On the other hand, the
338 PBM/GOM ratios at WLG were relatively lower than the values observed from the other two
339 Tibetan sites (Fig.8). Generally, gas-particle partitioning of GOM and PBM is mainly controlled by
340 air temperature (Amos et al., 2012), however, no clear dependence of monthly PBM/GOM ratio on
341 monthly mean air temperature was observed, e.g., similar PBM/GOM ratios were observed between
342 the coldest months (December to February) and other seasons (Fig. 8). Besides, air masses travelling
343 heights at WLG did not show clear seasonal variations throughout the study period, indicating
344 elevated PBM concentrations at WLG in winter and the early spring were unlikely associated with
345 intrusions of free troposphere air masses. We thus conclude that gas-particle partitioning of GOM
346 was not likely the major cause of the elevated PBM at WLG.

347

348 4 Conclusions

349 This study presented the first full-year continuous speciated Hg data set and identified potential



350 sources causing high GEM and PBM at WLG in the Tibetan Plateau. Mean GEM level at WLG was
351 slightly higher than the background level of GEM in the Northern Hemisphere. Mean PBM level at
352 WLG was much higher compared with the reported values in remote areas in the Northern
353 Hemisphere. Seasonal variations in GEM concentration indicated that Hg emissions from
354 anthropogenic source regions and long-rang transport played important roles on the high GEM
355 levels at WLG. High PBM concentrations at WLG were observed in cold season, which were mainly
356 caused by dust aerosol sources from the desert and Gobi areas. Analysis from CWT and $\sum AAI$
357 northern Xinjiang, eastern Qinghai, southern Gansu, southwestern Shaanxi, western Inner Mongolia
358 of China and northern South Asia could be the main source areas of GEM, while southern Xinjiang,
359 southwestern Inner Mongolia, northern Gansu, western Qinghai and Tibet of China were likely the
360 source regions of PBM at WLG. Long-range transport of dust particles from desert and Gobi areas
361 contribute to the elevated PBM at WLG. The estimated PBM emissions from dust particles
362 suggested that dust from desert and Gobi areas are critical sources of PBM on regional to global
363 scales, which should be paid more attention in future studies.

364

365 **Acknowledgments**

366 This work is supported by the Strategic Priority Research Program (XDB40000000), Key
367 Research Program of Frontier Sciences (ZDBS-LY-DQC029) of CAS, the National Science
368 Foundation of China (41703134 and 41622305), and the K.C. Wong Education Foundation of CAS.
369 We also thank staffs in Waliguan GAW Baseline Observatory for field sampling assistance.

370

371 **Reference**

- 372 AMAP/UNEP, 2013. Geospatially Distributed Mercury Emissions Dataset 2010v1.
373 AMAP/UNEP (2018) Technical Background Assessment for the 2018 Global Mercury Assessment.
374 Amos, H.M., Jacob, D.J., Holmes, C.D., Fisher, J.A., Wang, Q., Yantosca, R.M., Corbitt, E.S., Galarneau,
375 E., Rutter, A.P., Gustin, M.S., Steffen, A., Schauer, J.J., Graydon, J.A., St Louis, V.L., Talbot, R.W.,
376 Edgerton, E.S., Zhang, Y., Sunderland, E.M. (2012) Gas-particle partitioning of atmospheric Hg(II) and
377 its effect on global mercury deposition. *Atmospheric Chemistry and Physics* 12, 591-603.
378 Ariya, P.A., Amyot, M., Dastoor, A., Deeds, D., Feinberg, A., Kos, G., Poulain, A., Ryjkov, A., Semeniuk,
379 K., Subir, M., Toyota, K. (2015) Mercury Physicochemical and Biogeochemical Transformation in the
380 Atmosphere and at Atmospheric Interfaces: A Review and Future Directions. *Chemical Reviews* 115,
381 3760-3802.
382 Chakraborty, L.B., Qureshi, A., Vadenbo, C., Hellweg, S. (2013) Anthropogenic Mercury Flows in India
383 and Impacts of Emission Controls. *Environmental Science & Technology* 47, 8105-8113.
384 Che, H.Z., Wang, Y.Q., Sun, J.Y. (2011) Aerosol optical properties at Mt. Waliguan Observatory, China.
385 *Atmospheric Environment* 45, 6004-6009.
386 Chen, P.F., Kang, S.C., Li, C.L., Zhang, Q.G., Guo, J.M., Tripathee, L., Zhang, Y.A., Li, G., Gul, C.,
387 Cong, Z.Y., Wan, X., Niu, H.W., Panday, A.K., Rupakheti, M., Ji, Z.M. (2019) Carbonaceous aerosol



- 388 characteristics on the Third Pole: A primary study based on the Atmospheric Pollution and Cryospheric
389 Change (APCC) network. *Environmental Pollution* 253, 49-60.
- 390 Chen, S.Y., Huang, J.P., Kang, L.T., Wang, H., Ma, X.J., He, Y.L., Yuan, T.G., Yang, B., Huang, Z.W.,
391 Zhang, G.L. (2017) Emission, transport, and radiative effects of mineral dust from the Taklimakan and
392 Gobi deserts: comparison of measurements and model results. *Atmospheric Chemistry and Physics* 17,
393 2401-2421.
- 394 Cheng, I., Zhang, L., Blanchard, P., Dalziel, J., Tordon, R. (2013) Concentration-weighted trajectory
395 approach to identifying potential sources of speciated atmospheric mercury at an urban coastal site in
396 Nova Scotia, Canada. *Atmospheric Chemistry and Physics* 13, 6031-6048.
- 397 Cheng, I., Zhang, L.M. (2017) Uncertainty Assessment of Gaseous Oxidized Mercury Measurements
398 Collected by Atmospheric Mercury Network. *Environmental Science & Technology* 51, 855-862.
- 399 Chiapello, I., Prospero, J.M., Herman, J.R., Hsu, N.C. (1999) Detection of mineral dust over the North
400 Atlantic Ocean and Africa with the Nimbus 7 TOMS. *Journal of Geophysical Research-Atmospheres*
401 104, 9277-9291.
- 402 D'Amore, F., Bencardino, M., Cinnirella, S., Sprovieri, F., Pirrone, N. (2015) Data quality through a web-
403 based QA/QC system: implementation for atmospheric mercury data from the global mercury
404 observation system. *Environmental Science-Processes & Impacts* 17, 1482-1491.
- 405 Driscoll, C.T., Mason, R.P., Chan, H.M., Jacob, D.J., Pirrone, N. (2013) Mercury as a Global Pollutant:
406 Sources, Pathways, and Effects. *Environmental Science & Technology* 47, 4967-4983.
- 407 Fain, X., Obrist, D., Hallar, A.G., Mccubbin, I., Rahn, T. (2009) High levels of reactive gaseous mercury
408 observed at a high elevation research laboratory in the Rocky Mountains. *Atmospheric Chemistry and*
409 *Physics* 9, 8049-8060.
- 410 Feng, X.B., Sommar, J., Gardfeldt, K., Lindqvist, O. (2000) Improved determination of gaseous divalent
411 mercury in ambient air using KCl coated denuders. *Fresenius Journal of Analytical Chemistry* 366, 423-
412 428.
- 413 Fu, X.W., Feng, X., Liang, P., Deliger, Zhang, H., Ji, J., Liu, P. (2012a) Temporal trend and sources of
414 speciated atmospheric mercury at Waliguan GAW station, Northwestern China. *Atmospheric Chemistry*
415 *and Physics* 12, 1951-1964.
- 416 Fu, X.W., Feng, X.B., Sommar, J., Wang, S.F. (2012b) A review of studies on atmospheric mercury in
417 China. *Science of the Total Environment* 421, 73-81.
- 418 Fu, X.W., Feng, X.B., Wang, S.F., Rothenberg, S., Shang, L.H., Li, Z.G., Qiu, G.L. (2009) Temporal and
419 spatial distributions of total gaseous mercury concentrations in ambient air in a mountainous area in
420 southwestern China: implications for industrial and domestic mercury emissions in remote areas in China.
421 *Science of the Total Environment* 407, 2306-2314.
- 422 Fu, X.W., Feng, X.B., Zhu, W.Z., Wang, S.F., Lu, J.L. (2008) Total gaseous mercury concentrations in
423 ambient air in the eastern slope of Mt. Gongga, South-Eastern fringe of the Tibetan plateau, China.
424 *Atmospheric Environment* 42, 970-979.
- 425 Fu, X.W., Maruszak, N., Heimbürger, L.E., Sauvage, B., Gheusi, F., Prestbo, E.M., Sonke, J.E. (2016)
426 Atmospheric mercury speciation dynamics at the high-altitude Pic du Midi Observatory, southern France.
427 *Atmospheric Chemistry and Physics* 16, 5623-5639.
- 428 Fu, X.W., Zhang, H., Yu, B., Wang, X., Lin, C.J., Feng, X.B. (2015) Observations of atmospheric mercury
429 in China: a critical review. *Atmospheric Chemistry and Physics* 15, 9455-9476.
- 430 Giglio, L., Randerson, J.T., van der Werf, G.R. (2013) Analysis of daily, monthly, and annual burned area
431 using the fourth-generation global fire emissions database (GFED4). *Journal of Geophysical Research-*



- 432 Biogeosciences 118, 317-328.
- 433 Gustin, M.S., Amos, H.M., Huang, J., Miller, M.B., Heidecorn, K. (2015) Measuring and modeling
434 mercury in the atmosphere: a critical review. *Atmospheric Chemistry and Physics* 15, 5697-5713.
- 435 Gustin, M.S., Dunham-Cheatham, S.M., Zhang, L. (2019) Comparison of 4 Methods for Measurement
436 of Reactive, Gaseous Oxidized, and Particulate Bound Mercury. *Environmental Science & Technology*
437 53, 14489-14495.
- 438 Herman, J.R., Bhartia, P.K., Torres, O., Hsu, C., Sefstor, C., Celarier, E. (1997) Global distribution of UV-
439 absorbing aerosols from Nimbus 7/TOMS data. *Journal of Geophysical Research-Atmospheres* 102,
440 16911-16922.
- 441 Huang, J., Kang, S., Yin, R., Ram, K., Liu, X., Lu, H., Guo, J., Chen, S., Tripathee, L. (2020) Desert dust
442 as a significant carrier of atmospheric mercury. *Environmental Pollution* 267, 115442.
- 443 Jonsson, S., Skyllberg, U., Nilsson, M.B., Lundberg, E., Andersson, A., Bjorn, E. (2014) Differentiated
444 availability of geochemical mercury pools controls methylmercury levels in estuarine sediment and biota.
445 *Nature Communications* 5.
- 446 Kim, P.R., Han, Y.J., Holsen, T.M., Yi, S.M. (2012) Atmospheric particulate mercury: Concentrations
447 and size distributions. *Atmospheric Environment* 61, 94-102.
- 448 Kubilay, N., Oguz, T., Kocak, M., Torres, O. (2005) Ground-based assessment of Total Ozone Mapping
449 Spectrometer (TOMS) data for dust transport over the northeastern Mediterranean. *Global*
450 *Biogeochemical Cycles* 19.
- 451 Lan, X., Talbot, R., Castro, M., Perry, K., Luke, W. (2012) Seasonal and diurnal variations of atmospheric
452 mercury across the US determined from AMNet monitoring data. *Atmospheric Chemistry and Physics*
453 12, 10569-10582.
- 454 Lin, H.M., Tong, Y.D., Yin, X.F., Zhang, Q.G., Zhang, H., Zhang, H.R., Chen, L., Kang, S.C., Zhang, W.,
455 Schauer, J., de Foy, B., Bu, X.G., Wang, X.J. (2019) First measurement of atmospheric mercury species
456 in Qomolangma Natural Nature Preserve, Tibetan Plateau, and evidence of transboundary pollutant
457 invasion. *Atmospheric Chemistry and Physics* 19, 1373-1391.
- 458 Lindberg, S.E., Brooks, S., Lin, C.J., Scott, K.J., Landis, M.S., Stevens, R.K., Goodsite, M., Richter, A.
459 (2002) Dynamic oxidation of gaseous mercury in the Arctic troposphere at polar sunrise. *Environmental*
460 *Science & Technology* 36, 1245-1256.
- 461 Loewen, M., Kang, S., Armstrong, D., Zhang, Q., Tomy, G., Wang, F. (2007) Atmospheric transport of
462 mercury to the Tibetan plateau. *Environmental Science & Technology* 41, 7632-7638.
- 463 Lyman, S.N., Cheng, I., Gratz, L.E., Weiss-Penzias, P., Zhang, L.M. (2020) An updated review of
464 atmospheric mercury. *Science of the Total Environment* 707.
- 465 Moulin, C., Chiapello, I. (2004) Evidence of the control of summer atmospheric transport of African dust
466 over the Atlantic by Sahel sources from TOMS satellites (1979-2000). *Geophysical Research Letters* 31.
- 467 Murphy, D.M., Hudson, P.K., Thomson, D.S., Sheridan, P.J., Wilson, J.C. (2006) Observations of
468 mercury-containing aerosols. *Environmental Science & Technology* 40, 3163-3167.
- 469 Obrist, D., Kirk, J.L., Zhang, L., Sunderland, E.M., Jiskra, M., Selin, N.E. (2018) A review of global
470 environmental mercury processes in response to human and natural perturbations: Changes of emissions,
471 climate, and land use. *Ambio* 47, 116-140.
- 472 Obrist, D., Moosmuller, H., Schurmann, R., Chen, L.W.A., Kreidenweis, S.M. (2008) Particulate-phase
473 and gaseous elemental mercury emissions during biomass combustion: Controlling factors and
474 correlation with particulate matter emissions. *Environmental Science & Technology* 42, 721-727.
- 475 Okamoto, S., Tanimoto, H. (2016) A review of atmospheric chemistry observations at mountain sites.



- 476 Progress in Earth and Planetary Science 3.
477 Pirrone, N., Cinnirella, S., Feng, X., Finkelman, R.B., Friedli, H.R., Leaner, J., Mason, R., Mukherjee,
478 A.B., Stracher, G.B., Streets, D.G., Telmer, K. (2010) Global mercury emissions to the atmosphere from
479 anthropogenic and natural sources. *Atmospheric Chemistry and Physics* 10, 5951-5964.
480 Prospero, J.M., Ginoux, P., Torres, O., Nicholson, S.E., Gill, T.E. (2002) Environmental characterization
481 of global sources of atmospheric soil dust identified with the Nimbus 7 Total Ozone Mapping
482 Spectrometer (TOMS) absorbing aerosol product. *Reviews of Geophysics* 40.
483 Seigneur, C., Vijayaraghavan, K., Lohman, K., Karamchandani, P., Scott, C. (2004) Global source
484 attribution for mercury deposition in the United States. *Environmental Science & Technology* 38, 555-
485 569.
486 Selin, N.E. (2009) Global Biogeochemical Cycling of Mercury: A Review. *Annual Review of*
487 *Environment and Resources* 34, 43-63.
488 Sheu, G.R., Mason, R.P. (2001) An examination of methods for the measurements of reactive gaseous
489 mercury in the atmosphere. *Environmental Science & Technology* 35, 1209-1216.
490 Sprovieri, F., Pirrone, N., Bencardino, M., D'Amore, F., Carbone, F., Cinnirella, S., Mannarino, V., Landis,
491 M., Ebinghaus, R., Weigelt, A., Brunke, E.G., Labuschagne, C., Martin, L., Munthe, J., Wangberg, I.,
492 Artaxo, P., Morais, F., Barbosa, H.D.J., Brito, J., Cairns, W., Barbante, C., Dieguez, M.D., Garcia, P.E.,
493 Dommergue, A., Angot, H., Magand, O., Skov, H., Horvat, M., Kotnik, J., Read, K.A., Neves, L.M.,
494 Gawlik, B.M., Sena, F., Mashyanov, N., Obolkin, V., Wip, D., Bin Feng, X., Zhang, H., Fu, X.W.,
495 Ramachandran, R., Cossa, D., Knoery, J., Maruszczak, N., Nerentorp, M., Norstrom, C. (2016)
496 Atmospheric mercury concentrations observed at ground-based monitoring sites globally distributed in
497 the framework of the GMOS network. *Atmospheric Chemistry and Physics* 16, 11915-11935.
498 Sun, R.Y., Sun, G.Y., Kwon, S.Y., Feng, X.B., Kang, S.C., Zhang, Q.G., Huang, J., Yin, R.S. (2020)
499 Mercury biogeochemistry over the Tibetan Plateau: An overview. *Critical Reviews in Environmental*
500 *Science and Technology*.
501 Torres, O., Bhartia, P.K., Herman, J.R., Ahmad, Z., Gleason, J. (1998) Derivation of aerosol properties
502 from satellite measurements of backscattered ultraviolet radiation: Theoretical basis. *Journal of*
503 *Geophysical Research-Atmospheres* 103, 17099-17110.
504 Tsamalis, C., Ravetta, F., Gheusi, F., Delbarre, H., Augustin, P. (2014) Mixing of free-tropospheric air
505 with the lowland boundary layer during anabatic transport to a high altitude station. *Atmospheric*
506 *Research* 143, 425-437.
507 Wang, X., Lin, C.J., Yuan, W., Sommar, J., Zhu, W., Feng, X.B. (2016) Emission-dominated gas
508 exchange of elemental mercury vapor over natural surfaces in China. *Atmospheric Chemistry and*
509 *Physics* 16, 11125-11143.
510 Wang, Y.Q., Zhang, X.Y., Draxler, R.R. (2009) TrajStat: GIS-based software that uses various trajectory
511 statistical analysis methods to identify potential sources from long-term air pollution measurement data.
512 *Environmental Modelling & Software* 24, 938-939.
513 Wright, L.P., Zhang, L.M., Cheng, I., Aherne, J., Wentworth, G.R. (2018) Impacts and Effects Indicators
514 of Atmospheric Deposition of Major Pollutants to Various Ecosystems - A Review. *Aerosol and Air*
515 *Quality Research* 18, 1953-1992.
516 Wu, Y., Wang, S.X., Streets, D.G., Hao, J.M., Chan, M., Jiang, J.K. (2006) Trends in anthropogenic
517 mercury emissions in China from 1995 to 2003. *Environmental Science & Technology* 40, 5312-5318.
518 Xu, W.Y., Xu, X.B., Lin, M.Y., Lin, W.L., Tarasick, D., Tang, J., Ma, J.Z., Zheng, X.D. (2018) Long-
519 term trends of surface ozone and its influencing factors at the Mt Waliguan GAW station, China - Part 2:



520 The roles of anthropogenic emissions and climate variability. *Atmospheric Chemistry and Physics* 18,
521 773-798.

522 Xuan, J., Liu, G.L., Du, K. (2000) Dust emission inventory in Northern China. *Atmospheric Environment*
523 34, 4565-4570.

524 Yin, X.F., Kang, S.C., de Foy, B., Ma, Y.M., Tong, Y.D., Zhang, W., Wang, X.J., Zhang, G.S., Zhang,
525 Q.G. (2018) Multi-year monitoring of atmospheric total gaseous mercury at a remote high-altitude site
526 (Nam Co, 4730 m a.s.l.) in the inland Tibetan Plateau region. *Atmospheric Chemistry and Physics* 18,
527 10557-10574.

528 Zhang, B., Tsunekawa, A., Tsubo, M. (2008) Contributions of sandy lands and stony deserts to long-
529 distance dust emission in China and Mongolia during 2000-2006. *Global and Planetary Change* 60, 487-
530 504.

531 Zhang, H., Fu, X.W., Lin, C.J., Shang, L.H., Zhang, Y.P., Feng, X.B., Lin, C. (2016) Monsoon-facilitated
532 characteristics and transport of atmospheric mercury at a high-altitude background site in southwestern
533 China. *Atmospheric Chemistry and Physics* 16, 13131-13148.

534 Zhang, H., Fu, X.W., Lin, C.J., Wang, X., Feng, X.B. (2015a) Observation and analysis of speciated
535 atmospheric mercury in Shangri-La, Tibetan Plateau, China. *Atmospheric Chemistry and Physics* 15,
536 653-665.

537 Zhang, H., Fu, X.W., Wang, X., Feng, X.B. (2019) Measurements and Distribution of Atmospheric
538 Particulate-Bound Mercury: A Review. *Bulletin of Environmental Contamination and Toxicology* 103,
539 48-54.

540 Zhang, L., Wang, S.X., Wang, L., Wu, Y., Duan, L., Wu, Q.R., Wang, F.Y., Yang, M., Yang, H., Hao, J.M.,
541 Liu, X. (2015b) Updated Emission Inventories for Speciated Atmospheric Mercury from Anthropogenic
542 Sources in China. *Environmental Science & Technology* 49, 3185-3194.

543 Zhao, Z.Z., Cao, J.J., Shen, Z.X., Xu, B.Q., Zhu, C.S., Chen, L.W.A., Su, X.L., Liu, S.X., Han, Y.M.,
544 Wang, G.H., Ho, K.F. (2013) Aerosol particles at a high-altitude site on the Southeast Tibetan Plateau,
545 China: Implications for pollution transport from South Asia. *Journal of Geophysical Research-*
546 *Atmospheres* 118, 11360-11375.

547

548

549

550

551

552

553

554

555

556

557

558



559 **Figure Captions**

560 **Fig. 1:** The map showing the location of WLG, and distributions of the deserts and cities around
561 WLG.

562 **Fig. 2:** Time series of hourly GEM, GOM and PBM concentrations in ambient air at WLG.

563 **Fig. 3:** Monthly means of GEM, GOM and PBM at WLG during a full-year sampling period.

564 **Fig. 4:** Frequency distribution of wind direction and wind-sector based mean GEM and PBM
565 concentrations during the study period.

566 **Fig. 5:** Identified source regions of atmospheric GEM and PBM at WLG during the study period.
567 (A) gridded ($0.5^\circ \times 0.5^\circ$) values for GEM, and (B) gridded ($0.5^\circ \times 0.5^\circ$) values for PBM. Gray line
568 enclosed regions indicate desert locations in China.

569 **Fig. 6:** Correlation between the simulated GEM or PBM CWT value and their respective
570 anthropogenic emissions. The location of each gridded CWT value is matched with that of
571 anthropogenic emission. Gridded anthropogenic emissions are divided into 20 groups with equal
572 number of grids, starting from the lowest to highest emission values.

573 **Fig. 7:** Variations in daily mean PBM concentration and daily cumulative Absorbing Aerosol Index
574 (AAI) during the proceeding two days at WLG.

575 **Fig. 8:** The monthly PBM/GEM and PBM/GOM ratio with air temperature and air mass traveling
576 height during a full-year sampling period. Columns (a), (b) and (c) are the mean PBM/GEM and
577 PBM/GOM ratios at Qomolangma Natural Nature Preserve and Nam Co in the inland Tibetan
578 Plateau, Chinese cities and Chinese remote areas, respectively.

579

580

581

582

583

584

585

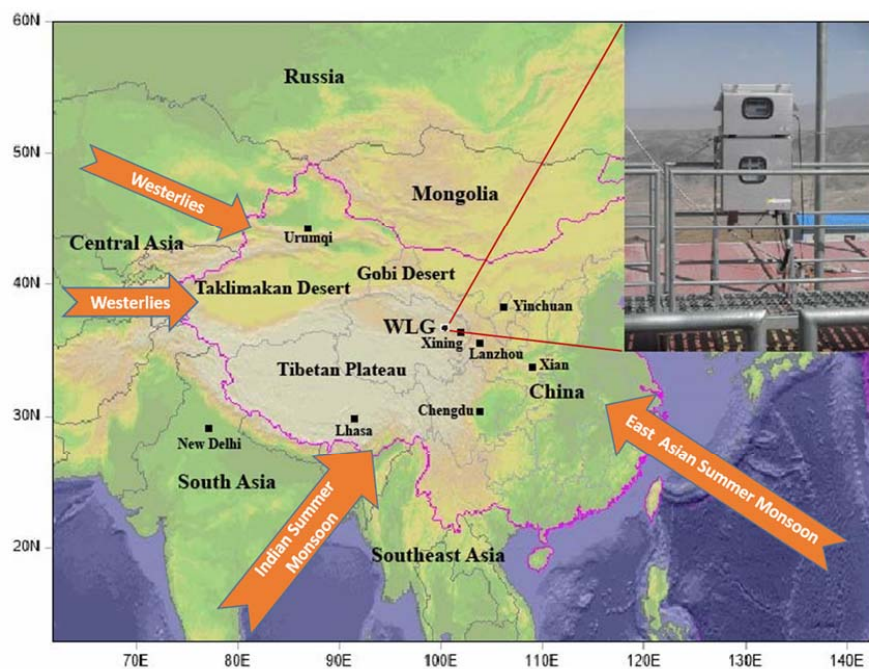
586

587

588



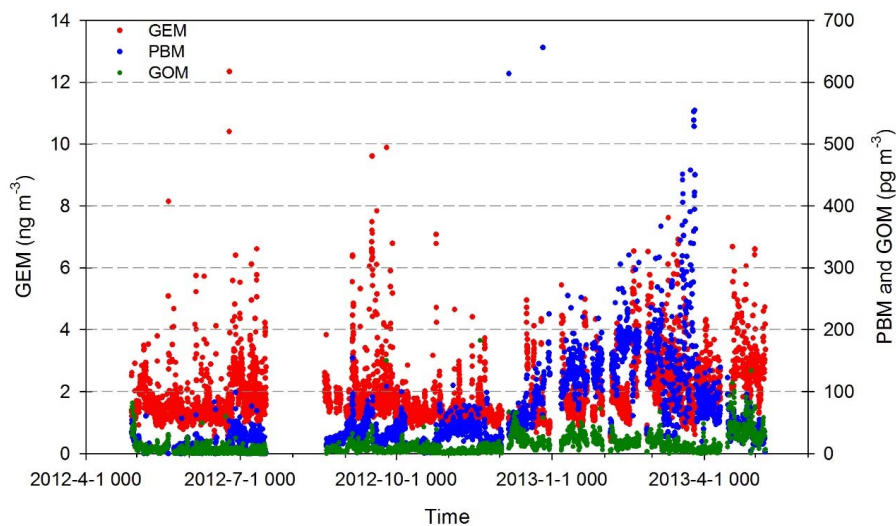
589 **Fig. 1:** The map showing the location of WLG, and distributions of the deserts and cities around
590 WLG.



591
592
593



594 **Fig. 2:** Time series of hourly GEM, GOM and PBM concentrations in ambient air at WLG.

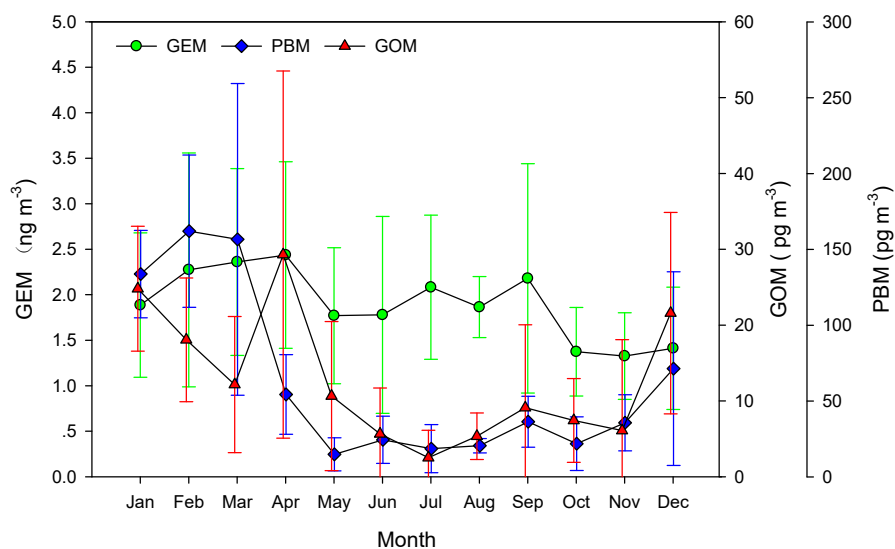


595

596



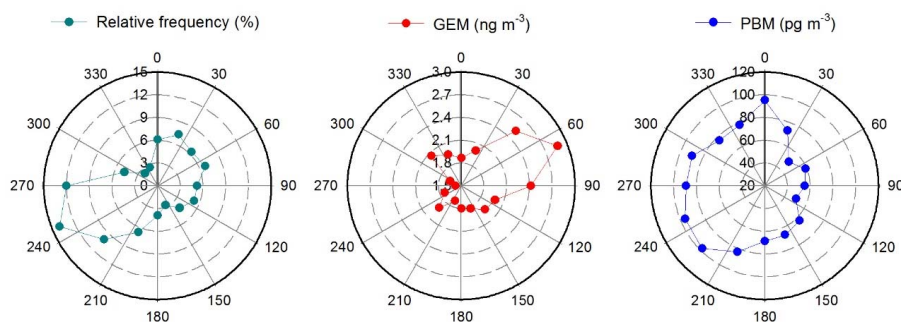
597 **Fig. 3:** Monthly means of GEM, GOM and PBM at WLG during a full-year sampling period.



598
599



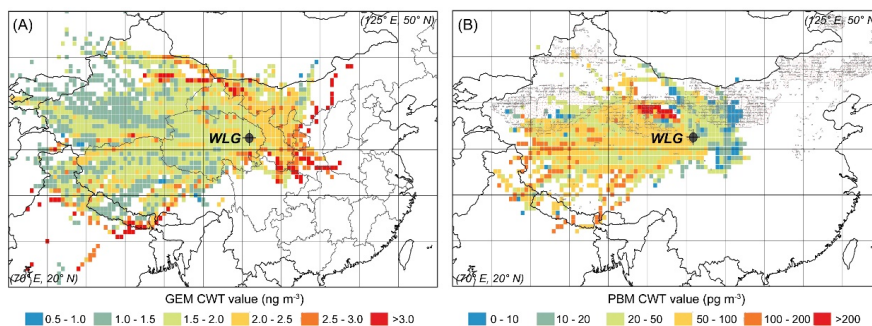
600 **Fig. 4:** Frequency distribution of wind direction and wind-sector based mean GEM and PBM
601 concentrations during the study period.



602
603
604



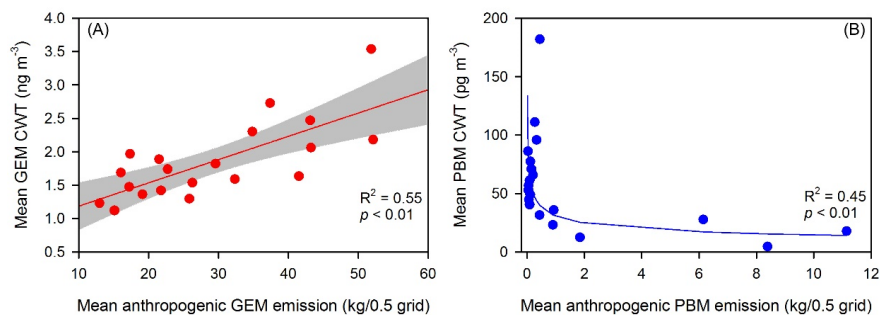
605 **Fig. 5:** Identified source regions of atmospheric GEM and PBM at WLG during the study period.
606 (A) gridded ($0.5^\circ \times 0.5^\circ$) CWT values for GEM, and (B) gridded ($0.5^\circ \times 0.5^\circ$) CWT values for PBM.
607 Gray line enclosed regions indicate desert locations in China.



608
609
610



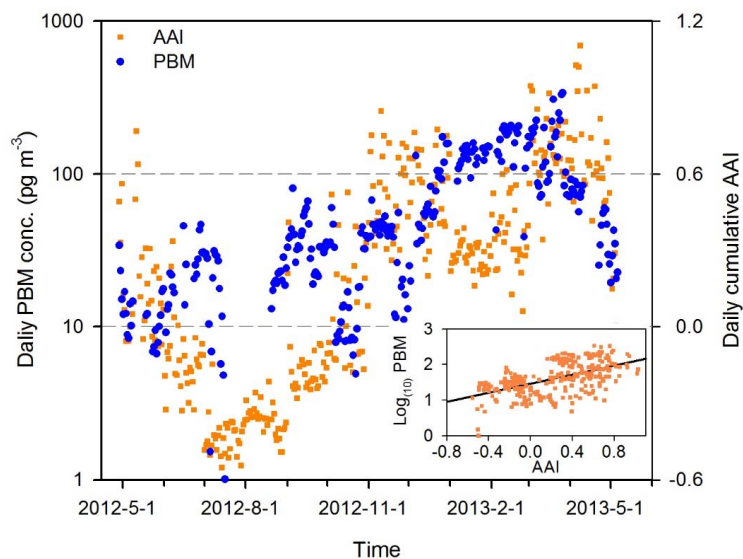
611 **Fig. 6:** Correlation between the simulated GEM or PBM CWT value and their respective
612 anthropogenic emissions. The location of each gridded CWT value is matched with that of
613 anthropogenic emission. Gridded anthropogenic emissions are divided into 20 groups with equal
614 number of grids, starting from the lowest to highest emission values.
615



616
617
618



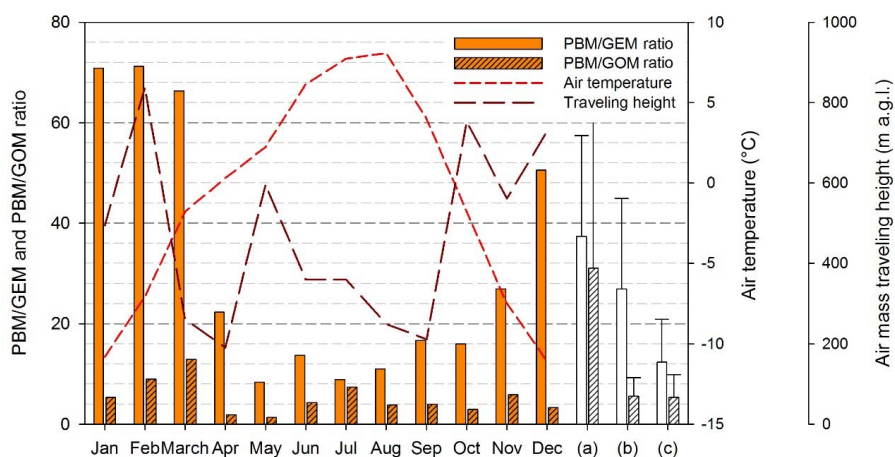
619 **Fig. 7:** Variations in daily mean PBM concentration and daily cumulative Absorbing Aerosol Index
620 (AAI) during the preceding two days at WLG.



621
622
623
624



625 **Fig. 8:** The monthly PBM/GEM and PBM/GOM ratio with air temperature and air mass traveling
626 height during a full-year sampling period. Columns (a), (b) and (c) are the mean PBM/GEM and
627 PBM/GOM ratios at Qomolangma Natural Nature Preserve and Nam Co in the inland Tibetan
628 Plateau, Chinese cities and Chinese remote areas, respectively.



629
630
631